Multi-criteria optimization and thermo-economic analysis of a heat pump-organic Rankine cycle Carnot battery system

Qiao, Hongna; Yu, Xiaohui; Kong, Weiqiang; Baniasadi, Ehsan; Yang, Bin

Published in:
Green Energy and Resources

Link to article, DOI:
10.1016/j.gerr.2023.100045

Publication date:
2023

Document Version
Publisher's PDF, also known as Version of record

Green Energy and Resources 1 (2023) 100045

Contents lists available at ScienceDirect

Green Energy and Resources

journal homepage: www.journals.elsevier.com/green-energy-and-resources

Research Article

Multi-criteria optimization and thermo-economic analysis of a heat pump-organic Rankine cycle Carnot battery system

Hongna Qiao [a], Xiaohui Yu [a,*], Weiqiang Kong [b], Ehsan Baniasadi [c], Bin Yang [a]

[a] Hebei Key Laboratory of Thermal Science and Energy Clean Utilization, Hebei, School of Energy and Environment Engineering, Hebei University of Technology, Tianjin 300401, China
[b] Department of Civil and Mechanical Engineering, Technical University of Denmark, Denmark
[c] Department of Mechanical Engineering, Faculty of Engineering, University of Isfahan, Iran

ARTICLE INFO

Keywords:
Rankine-based Carnot battery
Thermal-economic analysis
Single-objective optimization
Multi-objective optimization

ABSTRACT

Energy storage is a crucial solution for the intermittency and instability of renewable energy. Carnot batteries, a novel electrical energy storage technology, promise to address the challenges of renewable electrical energy storage worldwide. Rankine-based Carnot batteries, which are geographically unconstrained and effectively store energy at low temperatures, have attracted considerable attention in recent years. In this study, a mathematical model was developed, and a multi-objective optimization with power-to-power-efficiency, exergy efficiency, and levelized cost of storage was performed. Moreover, the investment cost and exergy loss of the optimized system components were investigated in detail and analyzed. The results showed that the optimal power-to-power-efficiency, exergy efficiency, and levelized cost of the storage system can be achieved at 60.3%, 33%, and 0.373 $/kWh based on single-objective optimization, and the operating parameters of the proposed system are different. Therefore, there is a strong trade-off relationship between the three objective functions mentioned above. Under the same weighting for the two approaches, they are 25.8%, 23%, and 0.437 $/kWh, and 39.3%, 29.1%, and 0.549 $/kWh, respectively. Furthermore, this study observed that the exergy destruction in the charge mode was nearly 95 kW larger than that in the discharge mode, and the exergy destruction of the throttle valve was the largest at 95.83 kW, accounting for 28.32%. The expander was the component with the highest cost (35.84% of the total cost) in the proposed system, followed by the compressor.

1. Introduction

Global warming has contributed to rising sea levels, melting glaciers, snow, and growing extreme weather (AghaKouchak et al., 2020), jeopardizing the balance of natural ecosystems, negatively affecting human health (Zhao et al., 2021), and even threatening the survival of human beings. In recent years, global energy has developed with great efficiency, cleanliness, and diversification to cope with global warming and reduce greenhouse gas emissions. There has been a rapid increase in the energy transition toward decarbonization in many countries worldwide. In this respect, the Chinese government has also proposed a "dual--carbon" goal (Jiang et al., 2022). The emergence of the "dual-carbon target" has promoted the development of renewable energy, yet the intermittent nature and instability of renewable energy have had great impacts on the security and stability of the power generation system (Li et al., 2018). Efficient energy storage technology is key to solving the problems associated with renewable energy storage.

Robert Laughlin stated that the Carnot battery (CB) will become a key storage technology for large amounts of energy in carbon-neutral energy systems. This technology is a promising solution for the global challenge of renewable electrical energy storage. Rankine-based CB has received widespread attention (Eppinger et al., 2021; Fan and Xi, 2022a; Jockenhöfer et al., 2018), which has the following advantages: (1) it can store sensible and latent heat and operates in a narrow temperature range (Liang et al., 2022); and (2) it has energy storage abilities at low temperatures with high energy density. These advantages are beneficial for heat loss and reservoir/machine material selection, as well as potentially permitting the selection of phase change materials as storage media (Dumont et al., 2020).

Studies on Rankine-based CB have mainly focused on several aspects: (1) screening of the working fluid, (2) configuration of the system, and

* Corresponding author.
E-mail address: 2018133@hebut.edu.cn (X. Yu).

https://doi.org/10.1016/j.gerr.2023.100045
Received 5 September 2023; Received in revised form 3 November 2023; Accepted 6 December 2023

Nomenclature

Acronyms

CB	Carnot battery
COP	coefficient of performance
GA	genetic algorithm
HP	heat pump
LCOS	levelized cost of storage ($/kWh)
ORC	organic Rankine cycle
P2P	power-to-power-efficiency
TES	thermal energy storage

Symbols

A	area (m^2)
C_{an}	annual operation cost ($)
C_{OM}	maintenance cost ($)
C_P	the standard equipment cost ($)
C_{PM}	the revised equipment cost ($)
C_{tot}	total initial investment cost ($)
Cl_i	proximity index
E_{com}	annual total electricity consumed (kWh)
E_{gen}	annual power generation (kWh)
E_r	exchange rate
E_x	exergy (kW)
Ex_D	exergy destruction (kW)
F	correction factor
F_{BM}	material correction factor
F_p	pressure correction factor
$\mathbf{g}(\boldsymbol{\chi})$	objective function
h	enthalpy (kJ/kg)
LT	service life (year)
m	mass flow (kg/s)
pr	electricity price ($/kWh)
P_{water}	price of water ($/kg)
Q	heat transfer rate (kW)
r	discount rate
R	recovery value
S_{i+}	the distance of the ideal
S_{i-}	the distance of the non-ideal
T	temperature (K)
v	design parameter
W	power (kW)
W_i	weights
$\boldsymbol{\chi}$	optimization variable vector

Greek symbols

η	efficiency
τ	storage duration (h)
ΔT_m	logarithmic average temperature

Subscripts

com	compressor
eva	evaporator
ex	exergy
exp	expander
hp	heat pump
hs	heat source
hx	heat exchanger
in	inlet
i	state point
low	lower
net	net generation
orc	Organic Rankine cycle
out	outlet
pump	working fluid pump
sto	thermal storage
thv	throttle valve
up	upper

(3) performance optimization. Pillai et al. (2019) theoretically analyzed 16 working fluids in the 4th generation refrigerants, where HFO-1336mzz(E) and R1234ze(Z) were identified as the most promising working fluids in this system because they have a low global warming potential and zero ozone depletion potential, as well as the minimum pressure drop required between the evaporator and condenser pressures. Furthermore, a thermodynamic model of organic-Rankine cycle (ORC) was developed in Python, and the generation efficiencies of the system were determined to be 7.58% and 8.83% when the working fluids were HFO-1336mzz(E) and R1234ze(Z), respectively. Eppinger et al. (2020) first surveyed and explored 33 working fluids based on the nature of the working fluid (dry, wet, and isentropic fluids) and realized that by selecting a dry fluid, the compressor discharge temperature would be greatly reduced and the coefficient of performance (COP) of the system would be increased, thereby boosting the power-to-power-efficiency (P2P) of the system. Subsequently, they (Steger et al., 2020) conducted an in-depth study of four dry fluids, namely, cyclopentane, R1233zd(E), Novec649, and R365mfc, and showed that the system using R1233zd(E) exhibits the best performances at the upper and lower thermal storage temperatures of 120°C and 90°C, respectively. Fan et al. (Fan and Xi, 2022b) studied R245fa and HFO-1336mzz(Z) from the perspective of working fluid pairs. The results showed that the system achieved the best economic performance with a minimum levelized cost of storage (LCOS) of 0.263 $/kWh when the former was applied to the ORC and the latter to the heat pump (HP).

Currently, the three main types of common Rankine-based CBs are the basic, reversible, and regenerator types. Dumont et al. (2015) verified the feasibility of reversible heat pump-organic Rankine cycle (HP-ORC) CB technology. Steger et al. designed a reversible HP-ORC CB (Steger et al., 2020) and developed computer-aided design modelling (Eppinger et al., 2021). This reversible system was analyzed by Staub et al. (2018), and numerical simulations revealed that the proposed system could deliver a P2P of 50% for small-scale applications. Fan et al. (Fan and Xi, 2022a) evaluated the thermo-economic performance of basic and added regenerator types. The results indicated that the system with a regenerator in both charge and discharge had better thermal and economic performance, whereas the system with a regenerator added to the charge had the highest P2P and exergy efficiencies of 25.06% and 19.12%, respectively. Su et al. (2023) developed four efficient geothermal-assisted CBs and the results showed that the heat-to-power efficiency was 20.54% ~85.73% higher than that of comparable CBs. Moreover, Alsagri et al. (Alsagri, 2023) proposed a system coupled with a CB with solar energy that could achieve P2P, power-to-process heat, and overall efficiencies of 26.82%, 55.78%, and 82.6% in optimized configurations, respectively. Tosun et al. (Canpolat Tosun et al., 2023) investigated the performance of a PV direct-drive-based CB under dynamic conditions. The results showed that the maximum COP of the heat pump system was 4.5, the exergy efficiency reached 78%, and the maximum sustainability index was 4.5.

To date, the optimization of system performance has focused on economic or thermodynamic performance. Fan et al. (Fan and Xi, 2022a) used the temperature and pressure at the compressor outlet and expander inlet as the optimization variables and the LCOS as the objective function. The optimal value of the LCOS of the system was determined using a single-objective genetic algorithm (GA), with the lowest LCOS of 0.29 $/kWh achieved for the system with a regenerator in both charge and

discharge modes. Zhang et al. (2022) identified the minimum value of LCOS for the Rankine-based CB with and without a regenerator using an artificial bee colony algorithm. The results showed that the LCOS reduced by nearly 10% with a regenerator in both charge and discharge modes, and the values of LCOS and minimum net investing cost can reach up to 0.293 $/kWh and 5.45 $\times$ 10^3 k$ when the thermal storage temperature is 120°C. In addition, studies have been conducted to optimize the thermodynamic performance of the system. Steger et al. (2020) used a multi-criteria decision-making method to determine the optimal thermal storage temperature (120°C for upper storage and 90°C for lower storage) for a reversible system. The P2P and storage capacities at the optimal thermal storage temperature were 59% and 3.6 kWh/t, respectively. Moreover, the trade-off between P2P and exergy efficiency was investigated and analyzed by Xue et al. (2022). The results revealed that the P2P and exergy efficiency could reach 97% and 64% under the heat source temperature and maximum thermal storage pressure, which were designed to be 87.1°C and 3.6 Mpa, respectively. Frate et al. (2020a) optimized these two system types with and without adding a regenerator, considering the P2P, exergy efficiency, and energy storage density. Finally, the optimal performance and key operational parameters of the system were determined. This study proved that the addition of a regenerator could improve the P2P and exergy efficiencies by 32% and 19%, respectively.

A review of these studies revealed that performance optimization is essential for improving system performance. The available studies on the performance optimization of Rankine-based CB focus primarily on a single thermodynamic or economic aspect. To the best of the authors' knowledge, Yu et al. (2022) and Niu et al. (2023) simultaneously considered the thermodynamic and economic performance in the optimization of the system. To the best of our knowledge, there is a knowledge gap about multi-objective optimization based on the three parameters, P2P, exergy efficiency, and LCOS, and in-depth analyses of the investment cost and exergy loss of the optimized system components. Therefore, a mathematical model was developed in this study, and multi-objective optimization was performed using these three metrics to exploit the performance potential and limitations of the proposed system. In addition, nine key operating parameters (evaporation temperature, condensation temperature, superheat temperature, upper and lower thermal storage temperatures, and outlet temperature of the heat source) were considered as optimization variables. Finally, the corresponding operating parameters under optimal operating conditions and theoretical design schemes were obtained, and the component cost and exergy destruction of the proposed system were analyzed and discussed.

2. System description

A schematic diagram of the Rankine-based CB, the HP-ORC CB, is shown in Fig. 1. It consists of the HP subsystem (red borderline), the TES subsystem (orange borderline), and ORC subsystem (blue borderline). The HP subsystem consisted of four main components: evaporator 1, condenser 1, compressor, and throttle valve. The ORC subsystem consisted of an evaporator, condenser, expander, and working-fluid pump. The TES subsystem connected the HP and ORC subsystems, which consisted of two pressurized water tanks and water pumps.

The operating mode of this system was divided into charging (HP), storage (TES), and discharging (ORC) modes. In the charging mode, the heat from the low-temperature heat source was absorbed by the working fluid in evaporator 1, and the working fluid was then compressed to a pressurized state. Subsequently, the high-temperature and high-pressure working fluid entered condenser 1 to transfer heat into the thermal storage medium. The thermal storage medium delivered heat to the H-tank during the storage period. Finally, the working fluid was throttled to the initial state at the throttle value and then flowed into evaporator 1. In the discharging mode, the working fluid absorbed the heat stored in evaporator 2. Then, it expanded in the expander, drove the generator to produce electric energy, and entered condenser 2 to throw off excess heat. Finally, it was pressurized by a working fluid pump and entered evaporator 2. The entire discharge period was completed.

3. Methodology

Fig. 2 shows the T-s diagram of the Rankine-based CB for the working fluid R1233zd (E), whose state points correspond to those in Fig. 1. The thermo-economic model of the Rankine-based CB was constructed using custom MATLAB, calling the thermodynamic and transport properties data of the working fluid in REFPROP 10.0. To study and analyze the performance of this system, mathematical models consisting of energy, exergy, and economic analyses were established based on the following assumptions.

(1) The proposed system operated stable operation (Yu et al., 2023).
(2) The pressure drop in the heat exchangers and pipes is negligible (Yu et al., 2023).
(3) A heat loss of 5 % is considered in the TES subsystem (Xue et al., 2022).
(4) R1233zd(E) was selected as the working fluid in this study based on previous studies (Eppinger et al., 2020; Steger et al., 2020).

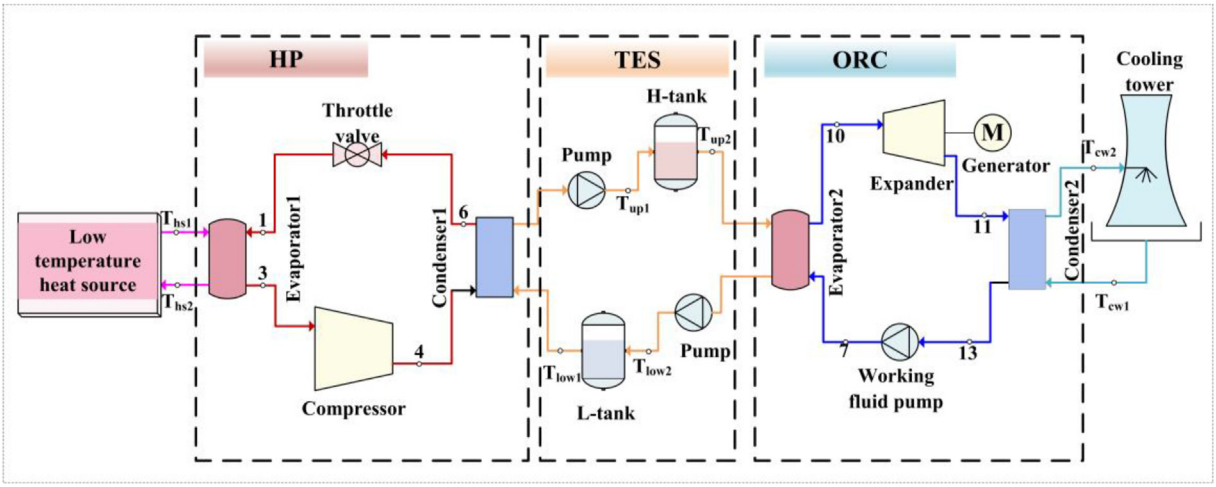

Fig. 1. The schematic diagram of the HP-ORC CB system.

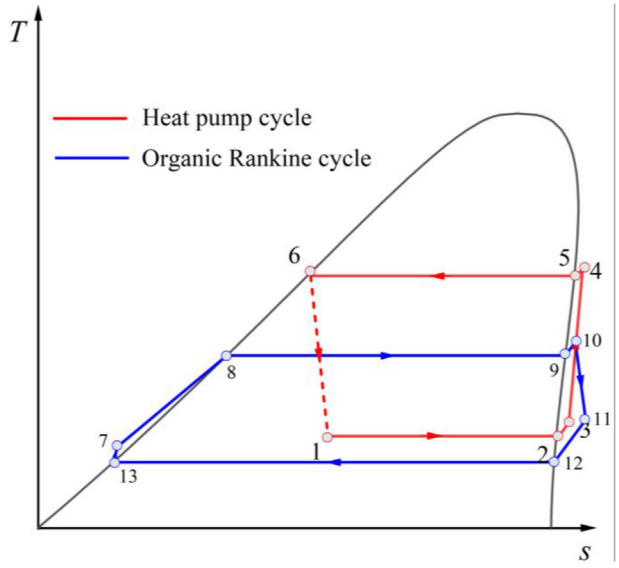

Fig. 2. T-s diagram of the Rankine-based CB.

3.1. Modeling

To obtain the optimal system performance and optimization of system circulation parameters, a series of boundary conditions of the Rankine-based CB were set and are listed in Table 1. The performance of the Rankine-based CB is affected by various parameters, such as the temperature of the heat source, the isentropic efficiency of the components, and the energy storage efficiency of the TES. These parameters were assumed constant, as listed in Table 1 (Frate et al., 2020a). In addition, the pinch point temperature difference depends on the heat exchanger technology and the heat transfer fluid; the minimum pinch point temperature was set to 5°C in this study (Hu et al., 2021).

3.1.1. Energy model

The P2P is an important index for evaluating the energy efficiency of Rankine-based CB systems. It can be calculated as follows:

$$P2P = \eta_{sto}\eta_{orc}COP \tag{1}$$

where η_{sto} is the TES energy storage efficiency, which is set to 0.95 (Frate et al., 2020a). COP and η_{orc} are the coefficients of the HP and the efficiency of the ORC, respectively, which are determined by Eqs. (2)-(3).

$$COP = \frac{\Delta h_{cd,hp}}{\Delta h_{com,hp}} = \frac{h_{4a} - h_6}{h_{4a} - h_3} \tag{2}$$

Table 1
Boundary conditions of the Rankine-based CB.

Parameter	Symbol	Unit	Value
Mass flow rate of heating source	m_{hs}	kg/s	10
Heat source inlet temperature	$T_{in,hs}$	°C	80
Cooling water inlet temperature	$T_{in,cw}$	°C	20
Cooling water outlet temperature	$T_{out,cw}$	°C	30
Environmental reference temperature	T_0	°C	15
Minimum pinch point temperature difference	$\Delta T_{pp,\min}$	°C	5
Minimum inlet and outlet temperature difference	$\Delta T_{let,\min}$	°C	10
Minimum cycle temperature difference	$\Delta T_{cyc,\min}$	°C	10
Storage duration	τ	h	6
Energy storage efficiency	η_{sto}	–	0.95
Isentropic efficiency of expander	η_{exp}	–	0.85
Isentropic efficiency of compressor	η_{com}	–	0.80
Isentropic efficiency of working fluid pump	η_{pump}	–	0.70

$$\eta_{orc} = \frac{\Delta h_{exp,orc} - \Delta h_{pump,orc}}{\Delta h_{eva,orc}} = \frac{(h_{10} - h_{11a}) - (h_{7a} - h_{13})}{h_{10} - h_{7a}} \tag{3}$$

where $\Delta h_{cd,hp}$ and $\Delta h_{com,hp}$ are the enthalpy differences across the HP condenser and compressor, respectively. $\Delta h_{exp,orc}$, $\Delta h_{pum,orc}$, and $\Delta h_{eva,orc}$ are the enthalpy differences across the ORC expander, pump, and evaporator, respectively. h_i and h_{ia} are the enthalpies of state point i for the ideal and actual processes, respectively.

The enthalpies of state points 4, 7, and 10 for the actual process can be expressed as

$$h_{4a} = \frac{h_4 - h_3}{\eta_{com}} + h_3 \tag{4}$$

$$h_{7a} = \frac{h_7 - h_{13}}{\eta_{pump}} + h_{13} \tag{5}$$

$$h_{11a} = h_{10} - \eta_{exp}(h_{10} - h_{11}) \tag{6}$$

where η_{com}, η_{pump}, and η_{exp} are the isentropic efficiencies of the compressor, working-fluid pump, and expander, respectively.

3.1.2. Exergy model

Exergy is defined as the portion of energy that can be maximally transformed into work when the system reversibly changes from an arbitrary state to a state balanced with the environment (Xue et al., 2022). Exergy analysis can be used to evaluate the quality of the energetic conversion process of a Rankine-based CB system. The important exergy evaluation index of the Rankine-based CB is the system exergy efficiency η_{ex} can be calculated as

$$\eta_{ex} = \frac{Ex_{orc}}{Ex_{hp} + Ex_{hs}} = \frac{P2PEx_{hp}}{Ex_{hp} + Ex_{hs}} \tag{7}$$

where Ex_{hp} and Ex_{hs} are the exergy amounts absorbed or delivered by the heat source and HP, respectively. These were determined using Eqs. (8)-(9).

$$Ex_{hp} = \frac{Q_{eva,hp}}{COP - 1}\tau \tag{8}$$

$$Ex_{hs} = m_{hs}\tau[(h_{in,hs} - h_{out,hs}) - T_0(s_{in,hs} - s_{out,hs})] \tag{9}$$

where m_{hs} is the mass flow of the heat transfer fluid in the heat source and τ is the storage duration, which is assumed to be 6 h. $Q_{eva,hp}$ represents the heat transfer rate of the evaporator in the HP model, which can be written as follows:

$$Q_{eva,hp} = m_{hs}(h_{in,hs} - h_{out,hs}) \tag{10}$$

The exergy destruction of each component was obtained and is listed in Table 2 according to the exergy equilibrium for any control volume Eq. (11).

$$\sum Ex_{in} = \sum Ex_{out} + Ex_D \tag{11}$$

where Ex_{in} and Ex_{out} represent the input and output exergies, respectively. Ex_D is the exergy destruction. The exergy of the state point i can be

Table 2
Exergy destruction of each component.

Component	Exergy destruction
Heat exchanger	$Ex_{D,hx} = \sum Ex_{in,hx} - \sum Ex_{out,hx}$
Compressor	$Ex_{D,com} = Ex_3 - Ex_4 + m_{hp}\Delta h_{com,hp}$
Expander	$Ex_{D,exp} = Ex_{10} - Ex_{11} - m_{orc}\Delta h_{exp,orc}$
Working fluid pump	$Ex_{D,pump} = Ex_{13} - Ex_7 + m_{orc}\Delta h_{pump,orc}$
Throttle valve	$Ex_{D,thv} = Ex_6 - Ex_1$

calculated as

$$Ex_i = \dot{m}[(h_i - h_0) - T_0(s_i - s_0)] \tag{12}$$

3.1.3. Economic model

Economic benefits are one of the most important concerns in the development and application of Rankine-based CB technology. The LCOS quantifies the discounted cost per unit of discharged electricity and has proven to be an appropriate tool for cost comparison of electricity storage technologies (Schmidt et al., 2019). Therefore, the LCOS was selected to assess the economic performance of the Rankine-based CB system presented in this study and can be expressed as

$$LCOS = \frac{C_{tot} + \sum_{i=1}^{LT} \frac{C_{an}}{(1+r)^i}}{\sum_{i=1}^{LT} \frac{E_{gen}}{(1+r)^i}} \tag{13}$$

where C_{tot} is the total initial investment cost, calculated using Eq. (14). C_{an} represents the annual operation cost, including the maintenance cost, power supply cost, and recovery value. LT and r are the lifetime of the system and discount rate, which were assumed to be 25 years and 5% in this study, respectively (Yu et al., 2023).

The total initial investment cost C_{tot} can be expressed as

$$C_{tot} = \frac{\sum C_{PM} + C_{thv} + C_{\text{tank}} + C_{water}}{1 - C_{2019}} \tag{14}$$

where C_{PM} includes the initial investment costs of the heat exchangers, compressor, expander, and working fluid pump. C_{thv} , C_{tank} , C_{water}, and C_{2019} are the initial investment costs of the throttle valve, storage tanks, heat-storage fluid, and working fluid, respectively.

C_{PM} can be calculated using the module costing technique method as follows:

$$C_{PM} = C_P F_{BM} = C_P(B_1 + B_2 F_M F_P) \tag{15}$$

$$\log C_P = K_1 + K_2 \log v + K_3 (\log v)^2 \tag{16}$$

$$\log F_P = C_1 + C_2 \log P + C_3 (\log P)^2 \tag{17}$$

where C_P refers to the basic cost of the equipment. F_{BM} and F_P are the material and pressure correction factors, respectively. The correction factors in Eqs. (15)–(17) are presented in Table 3. v refers to the design parameters of a component, and its calculation formulas are listed in Table 4.

In Table 4, ΔT_m refers to the logarithmic average temperature of the heat exchangers, which is defined as

$$\Delta T_m = \frac{(T_{H,in} - T_{L,out}) - (T_{H,out} - T_{L,in})}{ln\frac{(T_{H,in} - T_{L,out})}{(T_{H,out} - T_{L,in})}} \tag{18}$$

The formula for calculating the initial investment cost in the other components can be expressed as

$$C_{thv} = 114.5 m_{hp} \tag{19}$$

$$C_{tank} = 167.19 Er \frac{3600 m_{sto} \tau}{\rho_{water}} \tag{20}$$

$$C_{water} = 3600 P_{water} m_{sto} \tau \tag{21}$$

where Er and P_{water} are the exchange rates of the Euro and US dollar and the price of water for industrial use, respectively. In this study, these values were assumed to be 1.1756 (Yu et al., 2023) and 0.0016 $/kg (Frate et al., 2020b), respectively.

The Chemical Engineering Plant Cost Index is used to obtain the time cost of the working fluid. The cost of the working fluid is assumed to be 2% of the total cost. C_{2019} was calculated as follows:

$$C_{2019} = C_{2001} \frac{CEPCI_{2019}}{CEPCI_{2001}} \tag{22}$$

where $CEPCI_{2019} = 652.9$, $CEPCI_{2001} = 394.3$ (Xi et al., 2021).

C_{an} can be expressed as

$$C_{an} = C_{OM} + 0.05 E_{com} - R \tag{23}$$

where C_{OM} is the maintenance cost corresponding to 1.5% of the initial investment cost. R refers to the recovery value, which was taken as 0.

E_{com} and E_{gen} are the annual total electricity consumed in the HP mode and annual total electricity generation in the ORC mode, respectively. These can be calculated using Eqs. (24) and (25).

$$E_{com} = 365 W_{com} \tau \tag{24}$$

$$E_{gen} = 365 W_{exp} \tau \tag{25}$$

3.2. Optimization method

GA is an algorithm based on C. R. Darwin's biological evolutionism of "survival of the fittest", which mimics the processes of natural selection (selection, crossover, and mutation) and reproduction (iteration) to obtain optimal individuals (Xi et al., 2017). It is widely used in

Table 4
Design parameter of the component.

Type	Component	Formula
Area (m^2)	Evaporator of HP	$A_{eva1} = \frac{m_{hp}(h_3 - h_1)}{639 \Delta T_{m,eva1}}$
	Condenser of HP	$A_{con1} = \frac{m_{hp}(h_{4a} - h_6)}{653 \Delta T_{m,con1}}$
	Evaporator of ORC	$A_{eva2} = \frac{m_{orc}(h_{10} - h_{7a})}{639 \Delta T_{m,eva2}}$
	Condenser of ORC	$A_{con2} = \frac{m_{orc}(h_{11a} - h_{13})}{653 \Delta T_{m,con2}}$
Power (kW)	Compressor	$W_{com} = m_{hp}(h_{4a} - h_3)/1000$
	Expander	$W_{exp} = m_{orc}(h_{10} - h_{11a})/1000$
	Working fluid pump	$W_{pump} = m_{orc}(h_{7a} - h_{13})/1000$

Table 5
Configurations of GA.

Parameter	Value
Population	800
Crossover probability	0.8
Mutation probability	0.2
Maximum number of iterations	500

Table 3
Correction factors for the calculation of the component.

Component	K_1	K_2	K_3	C_1	C_2	C_3	B_1	B_2	F_M	F_{BM}
Heat exchanger	4.3427	−0.3030	0.1634	−0.039	0.082	−0.012	1.63	1.66	1.35	/
Expander	2.7050	1.4400	−0.1770	/	/	/	/	/	/	6.2
Working fluid pump	3.8700	0.3160	0.1220	−0.245	0.259	−0.014	1.89	1.35	2.35	/
Compressor	2.2897	1.3604	−0.1027	/	/	/	/	/	/	2.2

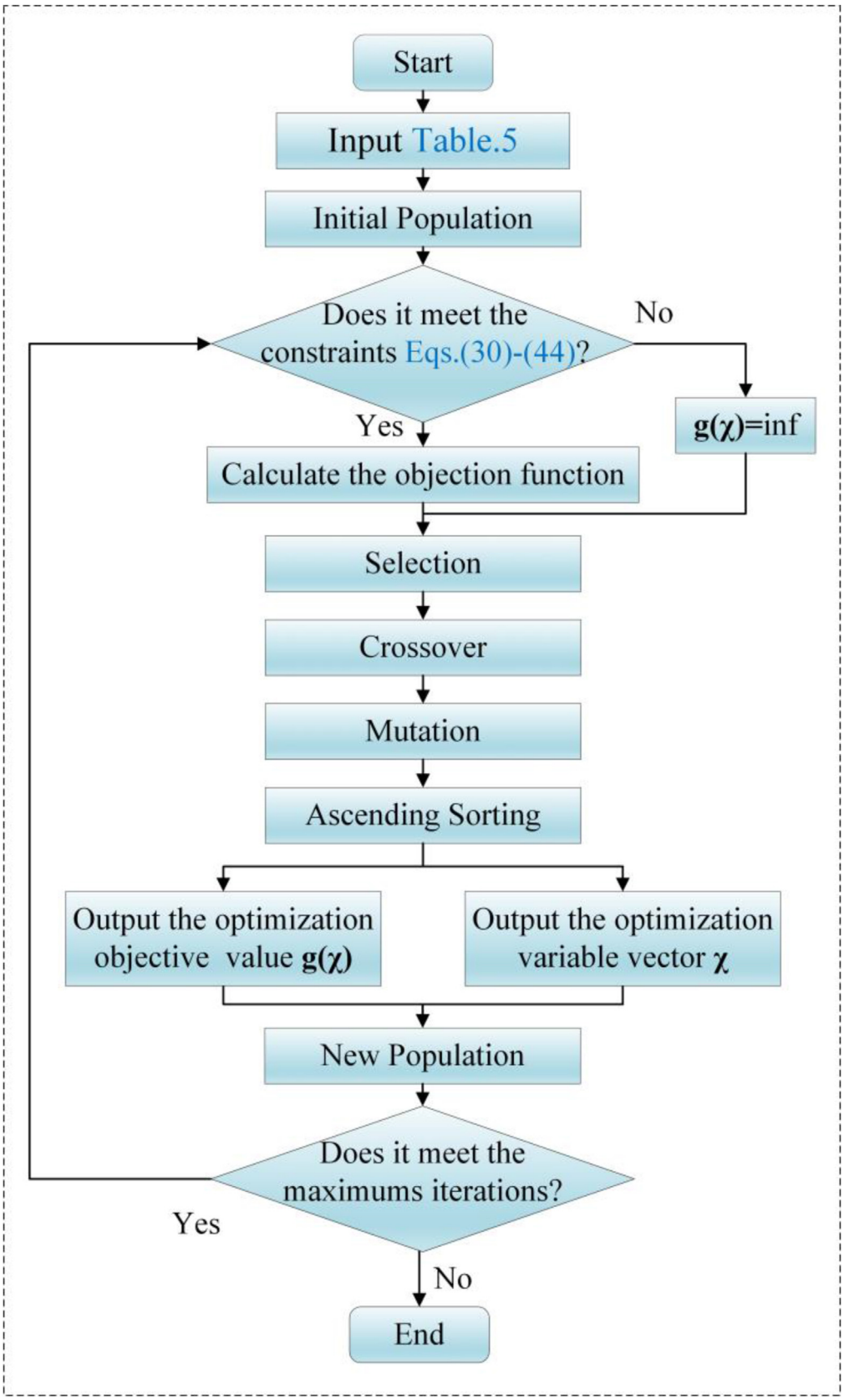

Fig. 3. GA flowchart of programming.

optimization projects. The thermodynamic and economic performances of Rankine-based CB depend on many key operating parameters. To achieve the single-indicator optimum of the proposed system, the system operating parameters were optimized using a single-objective GA.

In addition, previous studies have found that it is difficult for all evaluation indicators to perform well simultaneously (Yu et al., 2023). Therefore, multi-objective optimization is considered a trade-off between P2P, η_{ex}, and LCOS. When the optimal trade-off between the three indicators is studied, the objective function becomes a vector function. One approach is to "scalarize" the problem by converting it into a single-objective problem using the direct optimization results. The other approach uses a multi-objective GA-II to acquire the Pareto frontier; subsequently, the optimal result is obtained using the technique for order preference by similarity to an ideal solution (TOPSIS) decision-making method. In this study, these two approaches were selected for the multi-objective optimization process. The GA configurations are listed in Table 5; the corresponding programming flowchart is shown in Fig. 3.

The design optimization problem of a Rankine-based CB system can be expressed as follows:

$$\min_{x\in\Phi\subseteq R^m} \mathbf{g}(\boldsymbol{\chi}) \tag{26}$$

where $\boldsymbol{\chi}$ is the optimization variable vector, Φ represents the feasible region of the variables, R^m is a subset defined by the constraint conditions, and m is the number of optimization variables, which was nine for the proposed system. $\mathbf{g}(\boldsymbol{\chi})$ represents the objective function, when the optimization problem is single objective, $\mathbf{g}(\boldsymbol{\chi})$ may be equal to $1-P2P$, $-\eta_{ex}$ or LCOS; and when the optimization problem is multi-objective, $\mathbf{g}(\boldsymbol{\chi})$ equals Y, and its expression is as follows:

$$Y=\left\{\begin{array}{c} W_{ia}\left(\frac{1-P2P}{1-P2P_{max}}\right)+W_{ib}\left(\frac{-\eta_{ex}}{-\eta_{ex,max}}\right)+W_{ic}\left(\frac{LCOS}{LCOS_{min}}\right); approachA \\ \\ [1-P2P,-\eta_{ex},LCOS]; approachB \end{array}\right\} \tag{27}$$

where W_i is the weight, and the four weight sets W_{1-4} were investigated using Eq. (28) (Frate et al., 2020a).

$$\left\{\begin{array}{l} W1=[1/3,1/3,1/3] \\ W2=[1/2,1/2,0] \\ W3=[1/2,0,1/2] \\ W4=[2/3,0,1/3] \end{array}\right. \tag{28}$$

The operation process of the Rankine-based CB system is shown in Fig. 2, the optimization variable vector ($\boldsymbol{\chi}$) can be written as follows:

$$\boldsymbol{\chi}=\left\{T_{out,hs},T_{e,hp},T_{c,hp},\Delta T_{sh,hp},T_{e,orc},T_{c,orc},\Delta T_{sh,orc},T_{up},T_{low}\right\} \tag{29}$$

where $T_{out,hs}$ is the heat source outlet temperature, $T_{e,hp}$, $T_{c,hp}$, $T_{e,orc}$, and $T_{c,orc}$ refer to the evaporation and condensation temperatures of HP and the evaporation and condensation temperatures of ORC, respectively. $\Delta T_{sh,orc}$ and $\Delta T_{sh,hp}$ were superheated in the evaporator under HP and ORC, respectively. where T_{up} and T_{low} represent the upper and lower thermal storage temperatures, respectively. To ensure the stability, security, and efficiency of the proposed system, lower and upper boundaries of the optimization variables were assumed, as listed in Table 6.

A range of linear and nonlinear constraints should be considered to ensure that the working fluid operates in the subcritical range and obeys the pinch-point temperature-difference requirements during heat transfer. In addition, the complete dry compression of the proposed system in the charging mode and the absence of corrosion on the expander in the discharging mode are constraints that should be considered for the operation of the proposed system. These constraints can be expressed by Eqs. (30)–(44).

$$T_{c,hp}-T_{e,hp}\geq \Delta T_{\mathrm{cyc,min}} \tag{30}$$

$$T_{e,orc}-T_{c,orc}\geq \Delta T_{\mathrm{cyc,min}} \tag{31}$$

$$\chi_{hp}\left(P_{c,hp};s_{4a}\right)\geq 1 \tag{32}$$

$$\chi_{orc}\left(P_{c,orc};s_{11a}\right)\geq 1 \tag{33}$$

$$T_{out,hs}-T_{e,hp}\geq \Delta T_{pp,\mathrm{min}} \tag{34}$$

$$T_{in,hs}-\left(T_{e,hp}+\Delta T_{sh,hp}\right)\geq \Delta T_{pp,\mathrm{min}} \tag{35}$$

$$T\left(P_{c,hp};s_{4a}\right)-T_{\mathrm{up}}\geq \Delta T_{pp,\mathrm{min}} \tag{36}$$

$$T_{c,hp}-T_{low}\geq \Delta T_{pp,\mathrm{min}} \tag{37}$$

$$T_{low}-T(P_{e,orc};s_{7a})\geq \Delta T_{pp,\mathrm{min}} \tag{38}$$

$$T_{up}-(T_{e,orc}+\Delta T_{sh,orc})\geq \Delta T_{pp,\mathrm{min}} \tag{39}$$

$$T(P_{c,orc};s_{11a})-T_{out,cw}\geq \Delta T_{pp,\mathrm{min}} \tag{40}$$

$$T_{c,orc}-T_{in,cw}\geq \Delta T_{pp,\mathrm{min}} \tag{41}$$

$$T_{c,hp}-T_{up}+\frac{\max\left[\left(h\left(P_{c,hp};s_{4a}\right)-h\left(P_{c,hp};\chi=1\right);0\right]}{\Delta h_{cd,hp}}\left(T_{up}-T_{low}\right)\geq \Delta T_{pp,\mathrm{min}} \tag{42}$$

$$T_{low}-T_{e,orc}+\frac{h(P_{e,orc};\chi=0)-h(P_{e,orc};s_{7a})}{\Delta h_{eva,orc}}\left(T_{up}-T_{low}\right)\geq \Delta T_{pp,\mathrm{min}} \tag{43}$$

$$T_{c,orc}-T_{out,cw}+\frac{\max[(h(P_{c,orc};s_{11a})-h(P_{c,orc};\chi=1);0]}{\Delta h_{cd,orc}}(T_{out,cw}-T_{in,cw})\geq \Delta T_{pp,\mathrm{min}} \tag{44}$$

Eq. (30) and Eq. (31) ensures that the HP and ORC modes are correctly constructed. Eq. (32) ensures that compression ends in the superheated vapor region (dry compression), and Eq. (33) guarantees that the expression ends in the superheated-vapor region (protecting the expander). Eqs. (34)–(44) ensure that the condensation and evaporation processes comply with the pinch-point requirements of the HP and ORC models.

The TOPSIS decision-making method is a comprehensive evaluation method commonly used to determine the best solution to multi-objective problems (Niu et al., 2023; Wu et al., 2020; Yu et al., 2022). To eliminate the different dimensions of the objectives, they were normalized using Eq. (45) in this study.

Table 6
Lower and upper boundaries of optimization variables (Frate et al., 2020a).

Variables	$\chi(1)$	$\chi(2)$	$\chi(3)$	$\chi(4)$	$\chi(5)$	$\chi(6)$	$\chi(7)$	$\chi(8)$	$\chi(9)$
lb_{sys} (°C)	15	15	25	5	30	20	5	90	80
ub_{sys} (°C)	70	65	165	10	165	80	10	165	165

$$NY_{ij}^{n}=\frac{NY_{ij}-\min(NY_{ij})}{\max(NY_{ij})-\min(NY_{ij})},\ (NY_{ij}=1-P2P,-\eta_{ex},LCOS) \tag{45}$$

The TOPSIS decision-making method first requires determining the ideal and non-ideal points, where NY_{ij}^{n} are both 0 for the ideal point and 1 for the non-ideal point. The optimal solution is the closest to the ideal point and farthest from the non-ideal point. Therefore, the distance of each point on the Pareto frontier from the ideal and non-ideal points is denoted by S_{i+} and S_{i-}, respectively, which are calculated as follows:

$$S_{i+}=\sqrt{\left((1-P2P)_{j}^{n}-0\right)^{2}+\left((-\eta_{ex})_{j}^{n}-0\right)^{2}+\left((LCOS)_{j}^{n}-0\right)^{2}} \tag{46}$$

$$S_{i-}=\sqrt{\left((1-P2P)_{j}^{n}-1\right)^{2}+\left((-\eta_{ex})_{j}^{n}-1\right)^{2}+\left((LCOS)_{j}^{n}-1\right)^{2}} \tag{47}$$

Finally, the proximity index Cl_i was calculated using Eq. (48). Cl_i was between zero and one; the larger its value, the better the optimization result.

$$Cl_{i}=\frac{S_{i-}}{S_{i+}+S_{i-}} \tag{48}$$

4. Results and discussion

Based on the models and methods presented above, the multi-criteria optimization and thermo-economic analysis of the Rankine-based CB can be further discussed. The main results can be divided into two sections: model validation (Section 4.1) and optimization (Section 4.2).

4.1. Model validation

To validate the accuracy of the mathematical models proposed in this study, the simulated results of the Rankine-based CB were compared with the data obtained by Hu et al. (2021) and Fan et al (Fan and Xi, 2022a). A comparison of the simulation results is presented in Table 7. As shown in Table 7, the LCOS exhibited a maximum relative error of 5%. The relative errors of all other parameters were below 5%. Therefore, a mathematical model for Rankine-based CB can be relied on with an acceptable accuracy.

4.2. Optimization results

In this section, the optimal value of the objective function and key operating parameters of the Rankine-based CB were obtained based on the GA. Moreover, the investment cost and exergy destruction of each component of the proposed system were further analyzed and discussed to provide a clear and comprehensive view of the various components.

4.2.1. Single-objective optimization result

In this study, the performance indicators (*P2P*, η_{ex}, and LCOS) to be optimized were deformed to minimize the ease of code writing; that is, the smaller they are, the superior their performance. The iteration process and corresponding optimization variable χ for the single-objective GA ($1-P2P$, $-\eta_{ex}$, or LCOS) are shown in Fig. 4. It is observed that the optimal values of $1-P2P$ and LCOS stabilize around 150 iterations, and the optimal value of objective function $-\eta_{ex}$ stabilizes after 250 iterations. According to Fig. 4, the optimal *P2P*, η_{ex}, and LCOS based on the single objective optimization were 60.3%, 33% and 0.373 $/kWh, respectively. The results of the single objective optimizations show that the corresponding operating parameters χ of the presented system were different under the optimal *P2P*, η_{ex}, and LCOS. This means that these values cannot be optimized concurrently.

As shown in Fig. 4(a), the evaporation and condensation temperatures in the charging and discharging modes at maximum P2P were 64, 98, 82, and 35°C, respectively. P2P depended upon COP and η_{orc}. In the charging mode, the increasing COP may be related to two aspects: (1) The drop in $T_{c,hp}$ reduces the enthalpy at the compressor outlet, decreasing the power consumption of the compressor, and it also reduces the enthalpy of the throttle valve inlet, leading to an increase in $\Delta h_{cd,hp}$; (2) The rise in $T_{e,hp}$ reduces the compressor's power consumption, thus improving the COP of HP. In the discharge mode, higher $T_{e,orc}$ and lower $T_{c,orc}$ boost more power generation, which leads to a higher η_{orc}. In addition, the evaporating and condensing temperatures were limited by $T_{out,hs}$, T_{up}, T_{low}, $T_{out,cw}$, and ΔT_{pp}. Therefore, the optimized operating parameters χ are reported in Fig. 4(a). Similarly, the η_{ex} was obtained according to Eq. (7), which is affected by P2P and $\frac{Ex_{hp}}{Ex_{hp}+Ex_{hs}}$. The optimization results in Fig. 4(b) show that the χ value was not much different from P2P, but was also not exactly the same. However, when the LCOS (objective function) is minimized (Fig. 4(c)), the operating parameters χ of the optimized system are distinctly changed compared with Fig. 4(a) and (b). According to Eq. (13), the LCOS can be identified by C_{tot} , $\sum_{i=1}^{LT}\frac{C_{an}}{(1+r)^{i}}$ and $\sum_{i=1}^{LT}\frac{E_{gen}}{(1+r)^{i}}$. When $T_{e,hp}$, $T_{c,hp}$, $T_{e,orc}$, and $T_{c,orc}$ were 64, 98, 82, 35 °C and 15, 154, 136, and 34°C, the values of the aforementioned were 1.32×10^{6} \$, 3.78×10^{5} \$, 1.48×10^{6} kWh and 1.54×10^{7} \$, and 6.17×10^{7} \$ and 2.07×10^{8} kWh, respectively. This study observed that the sum of the total initial investment cost and the 25-year period maintenance cost 45 times more than before, and the total power generation in 25 years was 140 times more than before, when the temperature difference (between $T_{e,hp}$ and $T_{c,hp}$) increased from 34 to 149°C in the charging mode and the temperature difference (between $T_{e,orc}$ and $T_{c,orc}$) increased from 47 to 102°C in the discharging mode. Therefore, the high temperature difference (above-mentioned) can effectively reduce the LCOS and improve the economy of the total proposed system.

Fig. 5 shows the exergy destruction of each component under a single-objective GA. As shown in Fig. 5(a), the exergy destruction of the total system in discharge mode (54%) was 6.36 kW higher than that in charge mode (46%) under the optimal condition of the presented system with the highest P2P. The two major components of the heat exchange process exhibited the highest exergy destruction in the discharge mode, amounting to 18.25 and 14.47 kW, respectively. This is due to the fact that the large temperature difference in the heat exchanger causes its high exergy destruction in the discharge mode. Fig. 5(b) illustrates the results optimized with the exergy efficiency. The percentage of exergy destruction in the charge/discharge modes was 50% for each during operation, and the maximum exergy destruction was the evaporation process in the discharge mode because the working fluid had a high subcooling in evaporator 2, as shown in Fig. 2. Fig. 5(c) shows the exergy destruction and investment cost of each component when the proposed system had an optimal LCOS. The exergy destruction of the component was derived from the throttle valve in the charging mode, accounting for 64.14% of the total exergy destruction. These results can be explained by the high temperature difference (between $T_{e,hp}$ and $T_{c,hp}$) in the proposed system, which leads to an increase in the exergy difference between the condenser outlet and the evaporator inlet.

Fig. 5 shows the cost and percentage of each component for a single optimization case. As shown in Fig. 5(a), a smaller difference between the

Table 7
Verification results of the model (Fan and Xi, 2022a; Hu et al., 2021).

Parameter	Reference	Present work	Relative error
$W_{com}(kW)$	1545	1545	0
$W_{net}(kW)$	789	779	1.3%
COP	4.96	4.99	0.6%
$\eta_{orc}(\%)$	10	10	0
P2P (%)	50.00	50.40	0.8%
$\eta_{ex}(\%)$	27.50	26.40	4%
LCOS ($/kWh)	0.395	0.417	5%

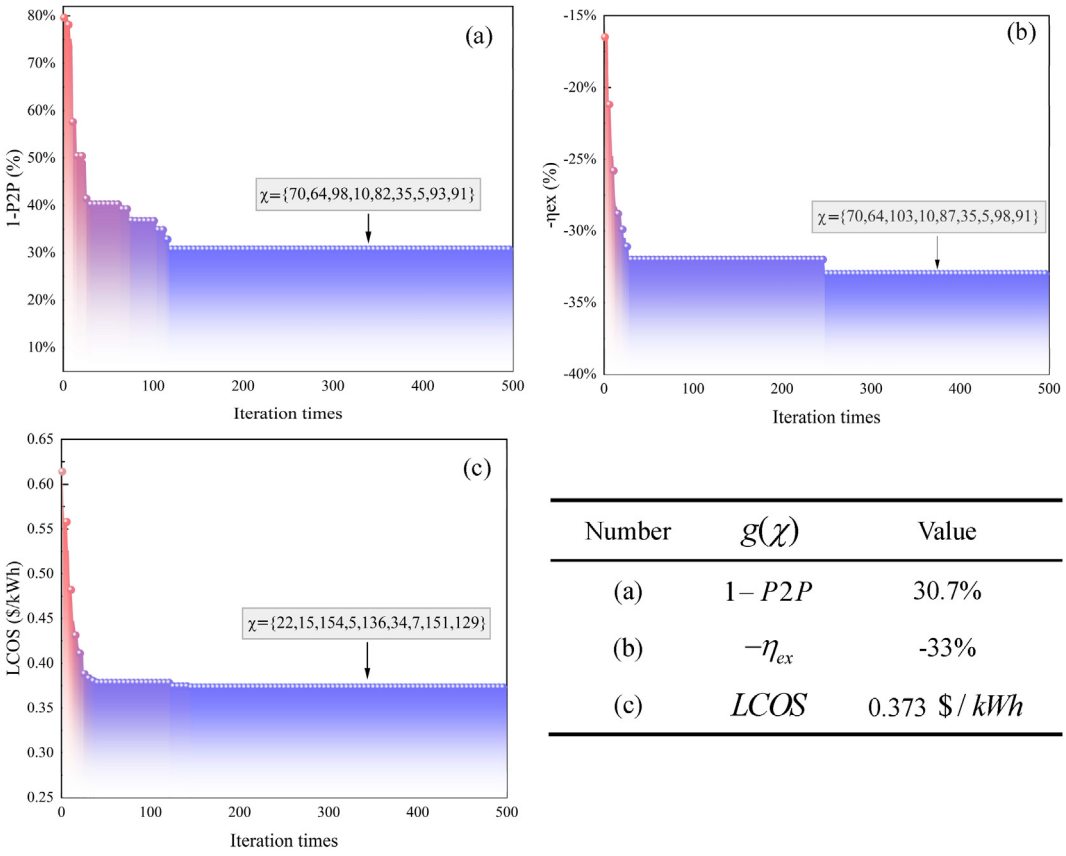

Number	$g(\chi)$	Value
(a)	$1-P2P$	30.7%
(b)	$-\eta_{ex}$	-33%
(c)	$LCOS$	0.373 $\$/kWh$

Fig. 4. Iterative process of a single-objective GA.

upper and lower thermal storage temperatures caused an increase in the mass flow rate of the heat storage medium. Consequently, the initial investment cost of the tanks increased to 487.73 k$ and accounted for 33.64% of the total initial investment cost of the system. As shown in Fig. 5(b) and (c), with the increase in thermal storage temperature difference (from 7 to 22°C), the cost of the tanks were 142.77 and 154.1 $/kWh, which were 70.1% and 68.4% lower than those of the tanks under the operating conditions of Fig. 5(a), respectively. Therefore, an appropriate thermal storage temperature difference plays a crucial role in reducing the initial investment costs of tanks.

4.2.2. Multi-objective optimization result

Based on Section 4.2.1, it is clear that the operating parameters of the proposed system differ when considering different objective functions, including P2P, η_{ex}, and LCOS. There was a strong trade off between the three indicators. The rising operating temperature difference can effectively improve the economic performance of the proposed system but deteriorates the energy conversion performance. Therefore, to simultaneously improve different performance metrics, including P2P, η_{ex}, and LCOS, two approaches were used to optimize these three-performance metrics in this study, and the optimization results are depicted in Figs. 6–10.

Figs. 6 and 7 display the iterative process of approach A ('multi-objective to single-objective') and the optimization results under different weights (W1–W4), respectively. The case in which P2P was ignored was not investigated because it was considered to have no practical significance (Frate et al., 2020a). From Fig. 7, the P2P, η_{ex}, and LCOS of the proposed system for W1 were 25.8%, 23%, and 0.437 $/kWh, respectively. In this case, the LCOS of the system reached a minimum value, while the low evaporation temperature of 35°C in the charging mode led to significantly low P2P (25.8%) and η_{ex} (23%), which negatively affected the proposed system. In the case of W2, which considered only energy and exergy, the P2P and η_{ex} of the proposed system were 157% and 43% higher than those of W1, respectively. This is because that the decreasing temperature difference between $T_{e,hp}$ and $T_{c,hp}$ from 103 to 38°C in the charging mode reduced the compressor power consumption and increased the COP, which led to a higher P2P and η_{ex}. Meanwhile, the LCOS of the proposed system as compared to those under other weights was maximized with a value of 0.806 $/kWh. As shown in Fig. 7, the results for the orange and pink lines were obtained based on P2P under different weights when P2P and LCOS were used as the objective functions. As the P2P weighting increased from 1/2 to 2/3, the P2P, η_{ex}, and LCOS of the proposed system increased by 34.5%, 25.5%, and 3.9%, respectively. This is because if the P2P weighting increases, the $T_{out,hs}$ and $T_{e,hp}$ of the proposed system increase, and the temperature difference between the T_{up} and T_{low} decreases. Consequently, the circulating temperature difference of the proposed system decreases, and the compressor power consumption decreases, enhancing the P2P of the system. However, the LCOS is affected by a combination of the initial investment cost, total maintenance cost, and total generation. As discussed in Section 4.2.1, the LCOS of the proposed system increased with the decrease in the temperature difference between the operating parameters of the system.

Figs. 8 and 9 show the 3D Pareto front results obtained using approach B and the values of the TOPSIS decision-making process. From Fig. 9, it can be clearly observed that the maximum Cl_i was 0.645 for a normalized $1-P2P$ of 0.229. No. 4 shows the corresponding number of optimal solutions (i.e., the key operating parameters of the system) in Fig. 10, marked by a black rectangle to visualize the optimal solution $\boldsymbol{\chi}$. It can also be observed from Fig. 8 that there is a normalized form of the

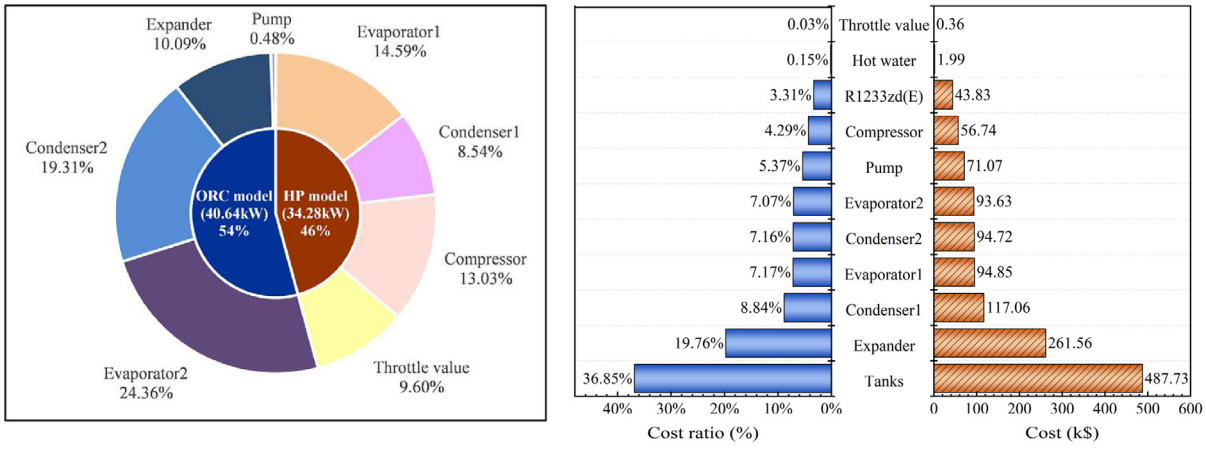

(a) a single-objective GA of *1 - P2P*

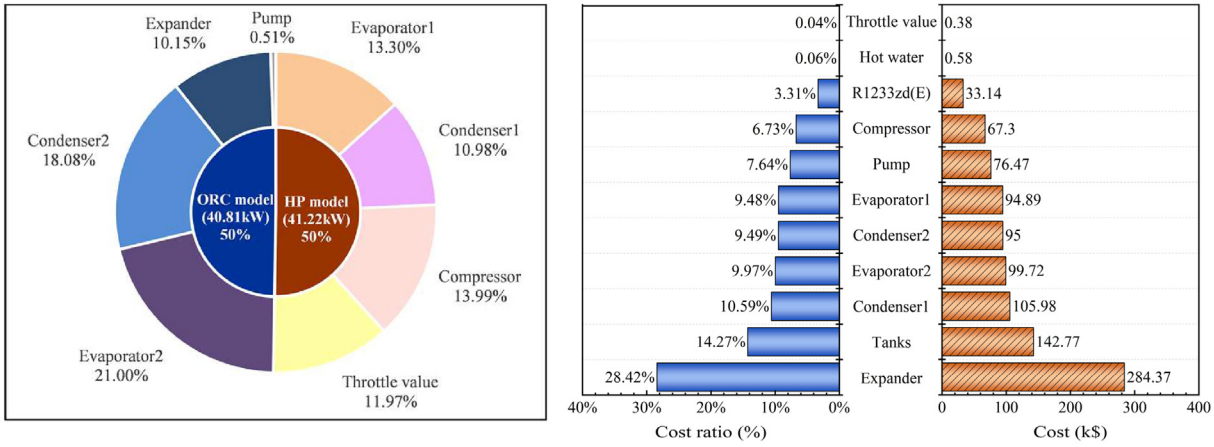

(b) a single-objective GA of $-\eta_{ex}$

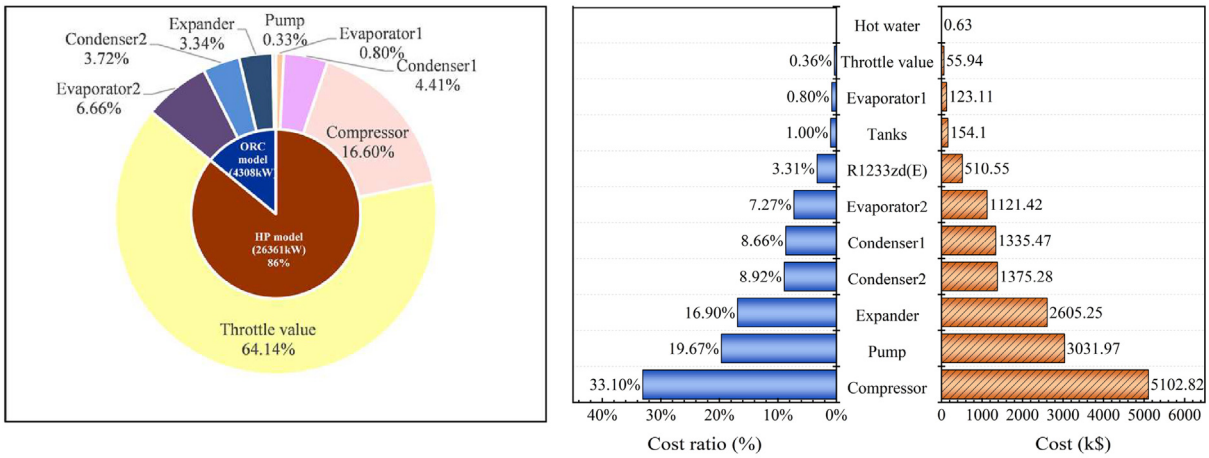

(c) a single-objective GA of *LCOS*

Fig. 5. (a) Exergy destruction and (b) cost of each component under optimal conditions with a single-objective GA.

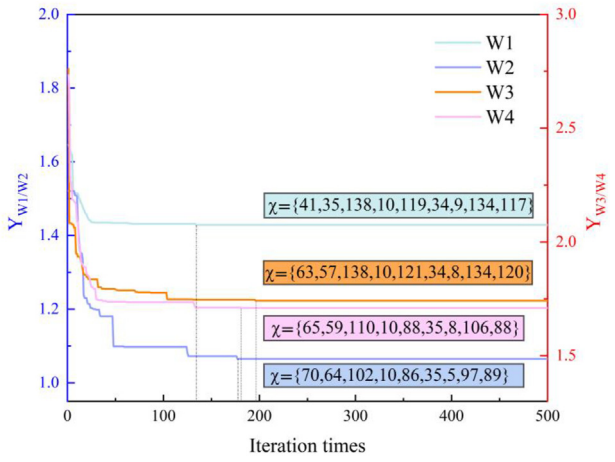

Fig. 6. Iterative process of a multi-objective GA with approach A.

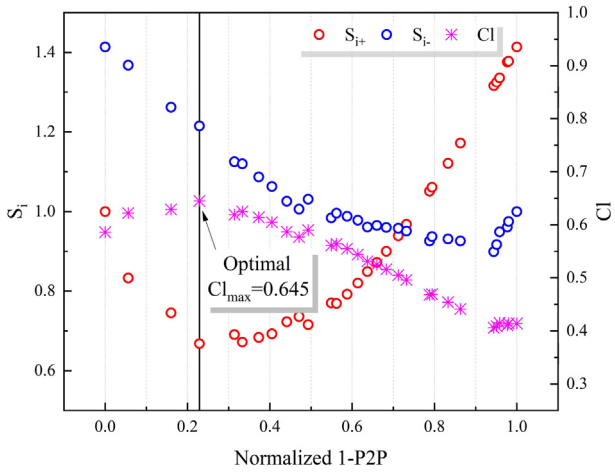

Fig. 9. The value in TOPSIS decision-making method.

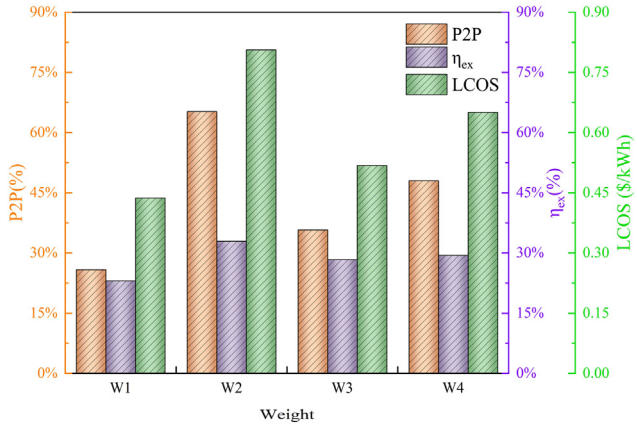

Fig. 7. Comparison of three objective functions under the four sets of weights $W1-4$.

Pareto frontiers, and the normalized optimization result is represented by a dark red blob. The corresponding P2P, η_{ex}, and LCOS of this dark red ball were 39.3%, 29.1%, and 0.549 $/kWh, respectively, which is clearly seen as a solution with all three objective functions located at the lower points. In the x-z projection plane, P2P was positively correlated with η_{ex} in most cases, indicating that η_{ex} is strongly influenced by P2P, and P2P and η_{ex} are monotonically negatively correlated with the economic cost in the x-y and x-z projection planes, respectively, indicating that the optimization of economic performance will result in the deterioration of the other two metrics. This implies that the proposed system cannot balance the thermal economy simultaneously, which is consistent with the results obtained by (Yu et al., 2022).

Figs. 11 and 12 depict the exergy destruction for each thermodynamic process and the cost of each component of the proposed system, respectively, under the optimized operating parameters of Approach A. As shown in Fig. 11, the exergy destruction of the system in the charging mode was significantly higher than that in the discharging mode under these four weights, and it exhibited the largest exergy destruction under the four weights, accounting for 44.21%,11.47%, 35.63%, and 16.93% of the total exergy destruction of the system, respectively. Therefore, the throttle performance should be improved to enhance the exergy of the proposed system. As shown in Fig. 12, the expander exhibited the highest investment cost of the proposed system under different weights, whereas hot water in the TES and throttling valve were the components with the lowest investment costs. Taking W2 as an example, the investment costs of the above three components were 279.84, 0.51, and 0.38 k$, accounting for 28.75%, 0.05%, and 0.04% of the total initial investment, respectively. According to Eqs. (15)–(17), the high investment cost of the

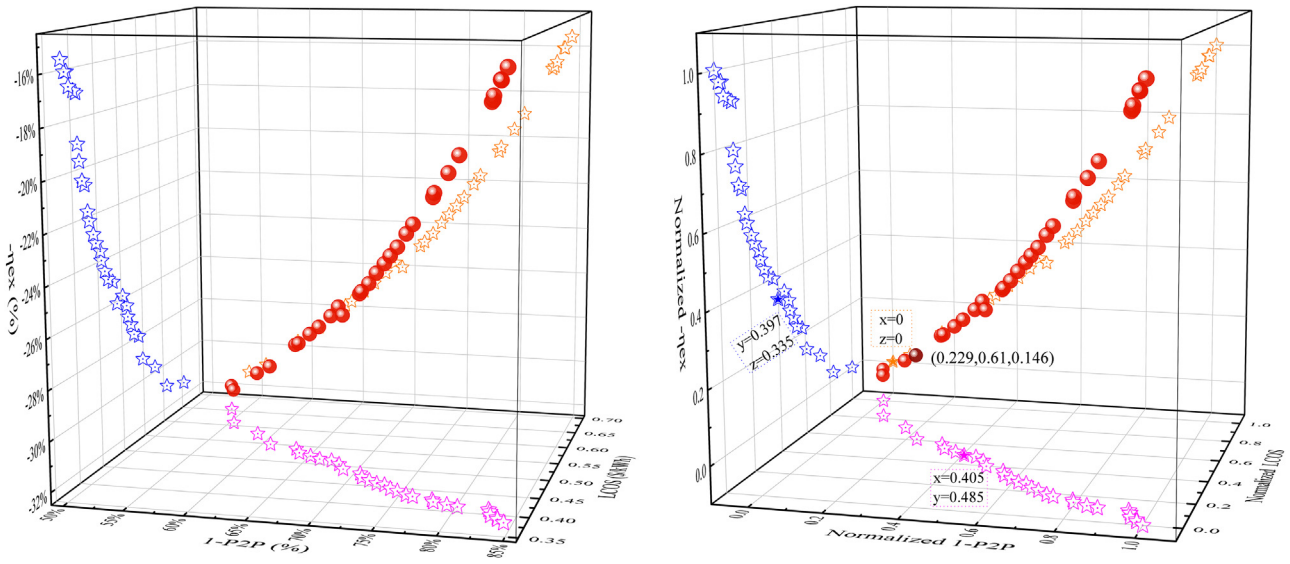

Fig. 8. Pareto frontier optimization result of a multi-objective GA with approach B.

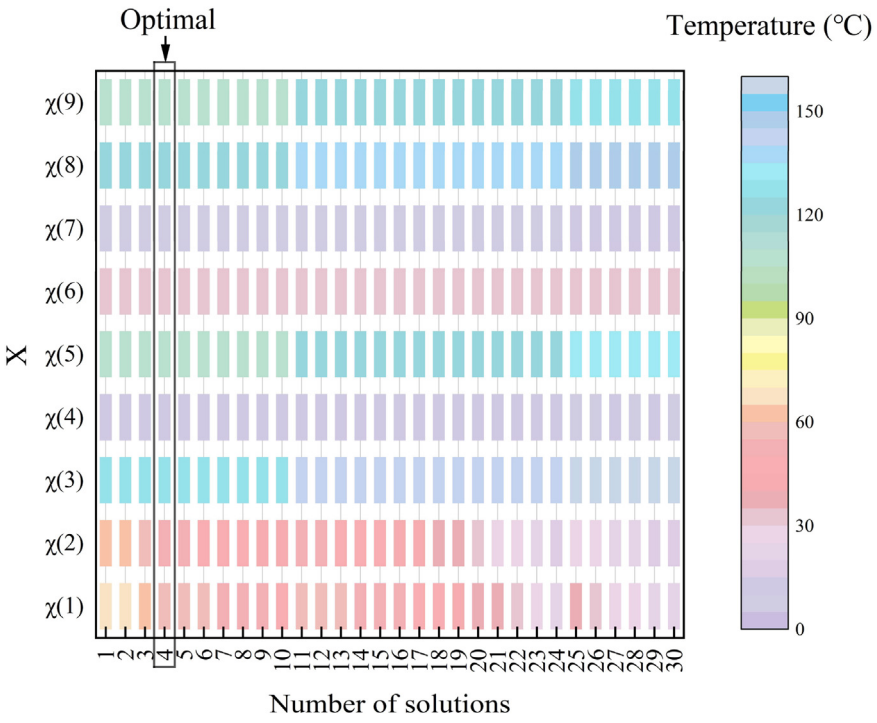

Fig. 10. Design specifications for the selected Pareto front configurations.

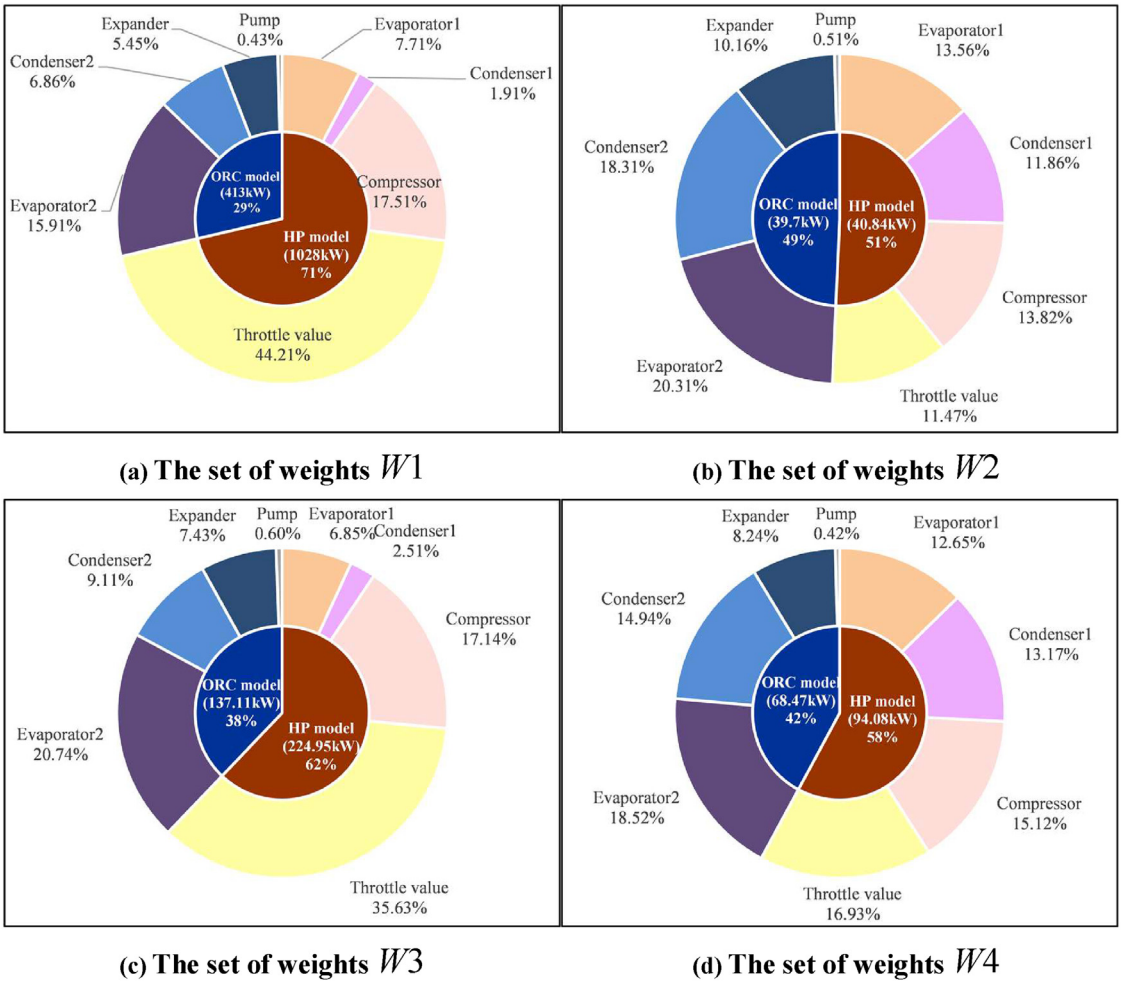

Fig. 11. Exergy destruction of each component under optimal conditions with approach A.

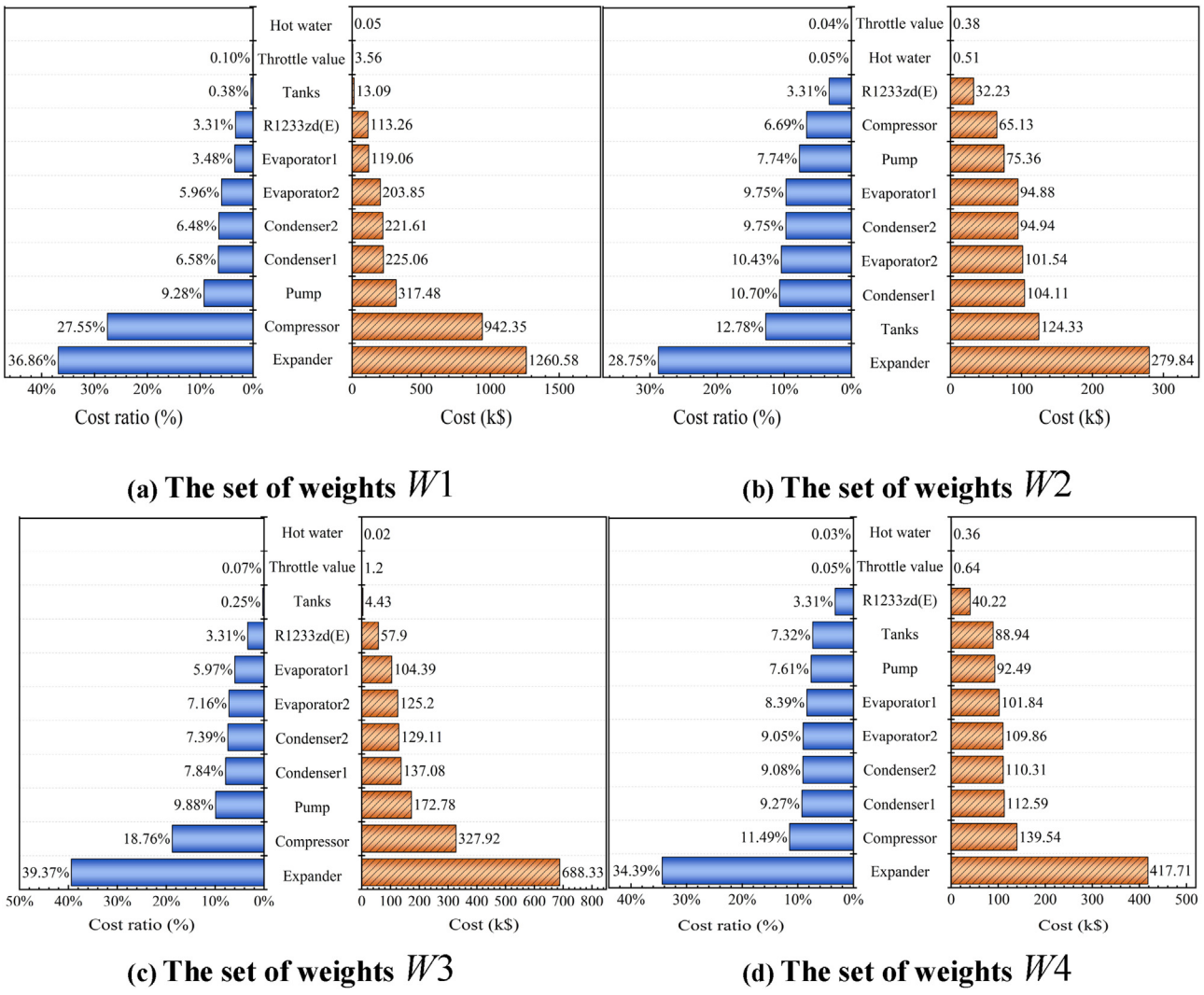

Fig. 12. The cost of each component under optimal conditions with approach A.

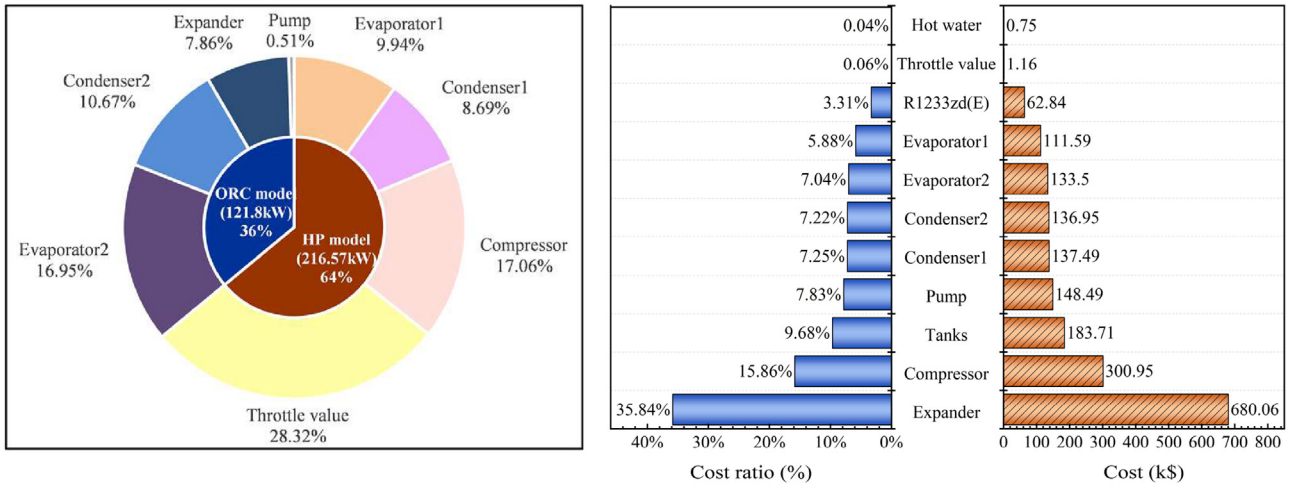

Fig. 13. Exergy destruction (a) and cost (b) of each component under optimal conditions with approach B.

expander was because of its high output power and relatively high operating pressure (Fan et al., 2022).

Fig. 13 shows the exergy destruction of each thermodynamic process and the cost of each component of the proposed system under the optimized operating parameters of Approach B. The exergy destruction in charge mode (64%) was approximately 95 kW greater than that in discharge mode (36%). The exergy destruction of the throttle value was the highest during the charging process, accounting for 28.32% of

the total exergy destruction. The corresponding exergy destructions of the evaporation and condensation processes in the discharging mode accounted for 16.95% and 10.67%, respectively. The above analysis shows that an increase in the temperature difference (between $T_{e,hp}$ and $T_{c,hp}$) resulted in the highest throttle loss, followed by the heat transfer process. Therefore, reducing the throttle loss and heat transfer loss will be the focus of our future research. Furthermore, as shown in Fig. 13, the two largest costs of the proposed system were the compressor and expander costs, which accounted for 15.86% and 35.84% of the total initial investment cost, respectively. Given the structural similarity of the compressor and expander, a compression and expansion dual-function machine should be taken into account for the proposed system to reduce the initial cost of the system, and this technology's feasibility has been demonstrated in (Wu et al., 2020).

5. Conclusions

In this study, the energy, exergy, and economy models of a Rankine-based CB system were built, and the performance parameters of the proposed system were optimized using a genetic algorithm. Single- and multi-objective optimizations were performed considering the P2P, exergy efficiency, and levelized cost of storage as objective functions. In addition, the exergy destruction and initial cost of the components and the total system were investigated and analyzed under optimal operating conditions. Based on the above analysis and discussion, the following conclusions were drawn.

1) The optimal P2P, exergy efficiency, and levelized cost of storage can be achieved at 60.3%, 33%, and 0.373 $/kWh, respectively, based on single-objective optimization of the proposed system.
2) For this proposed system, the optimal heat source outlet temperature was 59°C (between 15 and 70°C), which is closer to the maximum value; the optimal upper thermal storage temperature is 120°C (between 90 and 165°C), which is closer to the minimum value.
3) The optimal P2P, exergy efficiency, and levelized cost of storage with the same weighting for the two approaches were 25.8%, 23%, and 0.437 $/kWh and 39.3%, 29.1%, and 0.549 $/kWh, respectively.
4) The exergy destruction of the proposed system in the charge mode was nearly 95 kW larger than that in the discharge mode under the optimized operating parameters of approach B. The exergy destruction of the throttle value was the largest at 95.83 kW, accounting for 28.32%.
5) The compressor and expander exhibited the two largest initial costs of the proposed system, which amounted to 300.95 and 680.06 k$, and accounted for 15.86% and 35.84%, respectively. Thus, a dual-function compression and expansion machine should be considered for this system in follow-up work, which is extremely beneficial for reducing its initial investment cost and improving its economic performance.

Declaration of competing interest

The authors declare that they have no competing financial interests or personal relationships that may have influenced the work reported in this study.

Acknowledgements

This study was supported by the National Key R&D Program of China (No. 2022YFE0208300) and a grant from the Central Guiding Funds for Local Science and Technology Development Projects (No. 236Z4503G).

References

AghaKouchak, A., Chiang, F., Huning, L.S., et al., 2020. Climate extremes and compound hazards in a warming world. Annu. Rev. Earth Planet Sci. 48 (1), 519–548.
Alsagri, A., 2023. An innovative design of solar-assisted carnot battery for multigeneration of power, cooling, and process heating: techno-economic analysis and optimization. Renew. Energy 210.
Canpolat Tosun, D., Açıkkalp, E., Altuntaş, Ö., et al., 2023. Dynamic performance and sustainability assessment of a PV driven Carnot battery. Energy 278, 127769.
Dumont, O., Frate, G.F., Pillai, A., et al., 2020. Carnot battery technology: a state-of-the-art review. J. Energy Storage 32, 101756.
Dumont, O., Quoilin, S., Lemort, V., 2015. Experimental investigation of a reversible heat pump/organic Rankine cycle unit designed to be coupled with a passive house to get a Net Zero Energy Building. Int. J. Refrig. 54, 190–203.
Eppinger, B., Steger, D., Regensburger, C., et al., 2021. Carnot battery: simulation and design of a reversible heat pump-organic Rankine cycle pilot plant. Appl. Energy 288, 116650.
Eppinger, B., Zigan, L., Karl, J., et al., 2020. Pumped thermal energy storage with heat pump-ORC-systems: comparison of latent and sensible thermal storages for various fluids. Appl. Energy 280, 115940.
Fan, R., Xi, H., 2022a. Energy, exergy, economic (3E) analysis, optimization and comparison of different Carnot battery systems for energy storage. Energy Convers. Manag. 252, 115037.
Fan, R., Xi, H., 2022b. Exergoeconomic optimization and working fluid comparison of low-temperature Carnot battery systems for energy storage. J. Energy Storage 51, 104453.
Frate, G.F., Ferrari, L., Desideri, U., 2020a. Multi-criteria investigation of a pumped thermal electricity storage (PTES) system with thermal integration and sensible heat storage. Energy Convers. Manag. 208, 112530.
Frate, G.F., Ferrari, L., Desideri, U., 2020b. Rankine carnot batteries with the integration of thermal energy sources: a review. Energies 13.
Hu, S., Yang, Z., Li, J., et al., 2021. Thermo-economic analysis of the pumped thermal energy storage with thermal integration in different application scenarios. Energy Convers. Manag. 236, 114072.
Jiang, T., Yu, Y., Jahanger, A., et al., 2022. Structural emissions reduction of China's power and heating industry under the goal of “double carbon”: a perspective from input-output analysis. Sustain. Prod. Consum. 31, 346–356.
Jockenhöfer, H., Steinmann, W.-D., Bauer, D., 2018. Detailed numerical investigation of a pumped thermal energy storage with low temperature heat integration. Energy 145, 665–676.
Li, J., Liu, F., Li, Z., et al., 2018. Grid-side flexibility of power systems in integrating large-scale renewable generations: a critical review on concepts, formulations and solution approaches. Renew. Sustain. Energy Rev. 93, 272–284.
Liang, T., Vecchi, A., Knobloch, K., et al., 2022. Key components for Carnot Battery: technology review, technical barriers and selection criteria. Renew. Sustain. Energy Rev. 163, 112478.
Niu, J., Wang, J., Liu, X., et al., 2023. Optimal integration of solar collectors to Carnot battery system with regenerators. Energy Convers. Manag. 277, 116625.
Pillai, A., Kaya, A., De Paepe, M., et al., 2019. Performance Analysis of an Organic Rankine Cycle for Integration in a Carnot battery.
Schmidt, O., Melchior, S., Hawkes, A., et al., 2019. Projecting the future levelized cost of electricity storage technologies. Joule 3 (1), 81–100.
Staub, S., Bazan, P., Braimakis, K., et al., 2018. Reversible heat pump–organic rankine cycle systems for the storage of renewable electricity. Energies 11 (6), 1352.
Steger, D., Regensburger, C., Eppinger, B., et al., 2020. Design aspects of a reversible heat pump - organic rankine cycle pilot plant for energy storage. Energy 208, 118216.
Su, Z., Yang, L., Song, J., et al., 2023. Multi-dimensional comparison and multi-objective optimization of geothermal-assisted Carnot battery for photovoltaic load shifting. Energy Convers. Manag. 289, 117156.
Wu, Z., Sha, L., Zhao, M., et al., 2020. Performance analyses and optimization of a reverse Carnot cycle-organic Rankine cycle dual-function system. Energy Convers. Manag. 212, 112787.
Xi, H., Li, M.-J., He, Y.-L., et al., 2017. Economical evaluation and optimization of organic Rankine cycle with mixture working fluids using R245fa as flame retardant. Appl. Therm. Eng. 113, 1056–1070.
Xi, H., Li, M., Huang, Z., et al., 2021. Energy, exergy and economic analyses and performance assessment of a trigeneration system for power, freshwater and heat based on supercritical water oxidation and organic Rankine cycle. Energy Convers. Manag. 243, 114395.
Xue, X.J., Zhao, Y., Zhao, C.Y., 2022. Multi-criteria thermodynamic analysis of pumped-thermal electricity storage with thermal integration and application in electric peak shaving of coal-fired power plant. Energy Convers. Manag. 258, 115502.
Yu, X., Li, Z., Zhang, Z., et al., 2022. Energy, exergy, economic performance investigation and multi-objective optimization of reversible heat pump-organic Rankine cycle integrating with thermal energy storage. Case Stud. Therm. Eng. 38, 102321.
Yu, X., Qiao, H., Yang, B., et al., 2023. Thermal-economic and sensitivity analysis of different Rankine-based Carnot battery configurations for energy storage. Energy Convers. Manag. 283, 116959.
Zhang, Y., Xu, L., Li, J., et al., 2022. Technical and economic evaluation, comparison and optimization of a Carnot battery with two different layouts. J. Energy Storage 55, 105583.
Zhao, Q., Guo, Y., Ye, T., et al., 2021. Global, regional, and national burden of mortality associated with non-optimal ambient temperatures from 2000 to 2019: a three-stage modelling study. Lancet Planet. Health 5 (7), e415–e425.